

ARTICLES

Cation Distribution and Size-Strain Microstructure Analysis in Ultrafine Zn–Mn Ferrites Obtained from Acetylacetonato Complexes

Bratislav Antic*

Institute of Nuclear Sciences “Vinca”, Laboratory of Solid State Physics, Post Office Box 522, 11001 Belgrade, Serbia and Montenegro

Aleksandar Kremenović

Faculty of Mining and Geology, Laboratory for Crystallography, University of Belgrade, Post Office Box 162, 11001 Belgrade, Serbia and Montenegro

Aleksandar S. Nikolic

Faculty of Chemistry, Department for Inorganic Chemistry, University of Belgrade, Post Office Box 158, 11001 Belgrade, Serbia and Montenegro

Milovan Stoiljkovic

*Institute of Nuclear Sciences “Vinca”, Laboratory of Physical Chemistry, Post Office Box 522, 11001 Belgrade, Serbia and Montenegro**Received: July 29, 2003; In Final Form: February 17, 2004*

The ultrafine ZnFe_2O_4 , MnFe_2O_4 , and cation deficit Zn–Mn ferrites were obtained by thermal decomposition of appropriate mixed complex compounds with acetylacetone (2,4-pentadione) ligands ($[\text{M}(\text{AA})_x]$) at 500 °C. In ZnFe_2O_4 cation distribution is partially inverse with 14% of Zn^{2+} ions at octahedral 16d sites, while MnFe_2O_4 is a normal spinel. Cation distribution in nonstoichiometric $(\text{Zn,Mn,Fe})_{3-\delta}\text{O}_4$ ($\delta = 0.18\text{--}0.30$) is found to be $(\text{Zn}_x\text{Mn}_y\text{Fe}_{3-x-y}\text{O}_4)_{8a}[\text{Fe}_\delta\text{O}_\delta]_{16d}$, with a random distribution of vacancies. Nonstoichiometry in Zn–Mn ferrites is accompanied by a cation valence change, i.e., partial oxidation of Mn^{2+} to Mn^{4+} . Microstructure size-strain analysis shows isotropic X-ray line broadening due to the crystallite size effect and anisotropic X-ray line broadening due to the crystallite strain effect. In binary ferrites anisotropic X-ray line broadening due to the strain effect is higher in ZnFe_2O_4 than in MnFe_2O_4 , while in ternary cation-deficient Zn–Mn ferrites it decreases as the vacancy concentration δ increases.

1. Introduction

Fine-particle ferrites attract considerable interest due to their application in high-density magnetic recording media, as suspension materials in ferromagnetic liquids, and as catalysts. They can be applied directly onto PET films and papers to create prepaid cards and magnetic tickets.^{1,2} The interest in these materials permanently increases because of their usability under extreme conditions. They possess unique magnetic, chemical, and mechanical properties. It is well-known that properties of ferrite materials strongly depend on the preparation conditions. Consequently, different methods for preparation of ferrite powders are described in the literature.^{3–5} By choosing the method that reduces particle size dimension, magnetic properties such as coercive field, Curie temperature, and saturation magnetization may change significantly in comparison with the bulk material. One of the most interesting methods for prepara-

tion of ultrafine powders is from complex compounds as precursors. Since most metals make complexes with β -diketonato ligands, several ligands of this type were used for synthesis: acetylacetone (AA), benzoylacetone (BA), dibenzoylmethane (DBM), trifluoroacetone (TFA), etc.^{6,7} Prepared complexes have relatively low temperatures of thermal decomposition, giving ultrafine powder as a product.⁸

Ferrites with spinel structure, ZnFe_2O_4 , MnFe_2O_4 , and $(\text{Zn,Mn})\text{Fe}_2\text{O}_4$, are widely studied and used in technology. Bulk Zn ferrite is a normal spinel (space group $Fd\bar{3}m$) with Zn^{2+} at tetrahedral (8a) and Fe^{3+} at octahedral (16d) sites and it shows an antiferromagnetic ordering below 9 K.⁹ However, its nanosize powder has a mixed cation distribution with some percentage of Zn^{2+} at 16d sites, leading to different magnetic behavior.¹⁰ Bulk Mn ferrite has a mixed cation distribution with Mn^{2+} and Fe^{3+} at both crystallographic sites in a quantity that depends on sample preparation.¹¹ In Mn–Zn ferrites the cation distribution varies, depending on preparation route, stoichiometry, etc.^{11–13}

* To whom correspondence should be addressed: fax (381) 118065829; e-mail bantic@vin.bg.ac.yu.

The goal of this work is to apply a new synthetic route to prepare ultrafine Zn, Mn, and Zn–Mn ferrites by using complexes with acetylacetone ligands as precursors, and to investigate their structural and microstructural properties by X-ray powder diffraction (XRPD). Determination of structure parameters, especially cation distribution, is important in understanding and controlling magnetic properties. Electromagnetic properties also strongly depend on the microstructure, so its determination from the XRPD is also presented.

2. Experimental Details

2.1. Sample Preparation. ZnFe_2O_4 , MnFe_2O_4 , and Zn–Mn ferrites ($\text{Zn}_x\text{Mn}_{1-x}\text{Fe}_2\text{O}_4$) were synthesized by thermal decomposition of appropriate complexes $[\text{M}(\text{AA})_x]$, where M denotes the corresponding cation: Zn, Mn, or Fe. The complexes $[\text{M}(\text{AA})_x]$ were synthesized according to a previously described method.¹⁴ Thermal decomposition of the mixture of basic complexes was carried out in air, at a heating rate of 10 °C/min. The samples were held for 1 min at final temperature, $T = 500$ °C, and quickly cooled (20 °C/min). Phase composition of the products was checked by the XRPD method.

2.2. Elemental Analyses. The elemental analyses were performed by inductively coupled plasma atomic emission spectroscopy (ICP-AES), (Spectroflame, 2.5 kW, 27 MHz) and also tested by direct current argon-stabilized plasma arc emission spectroscopy (DCP-AES). The details of the DCP argon plasma arc device have been described elsewhere.¹⁵ Very good agreement of results was obtained.

Two fine powdered specimens for each ferrite analyzed are precisely weighed (~31 mg) and transferred into a glass crucible. Samples are dissolved by adding 5 mL of HCl (1 + 1) and gently heated on a hot plate. After dissolution, the solutions were transferred and diluted with distilled water to a volume of 100 mL. A portion of 5 mL of each solution obtained was taken, 1 mL of 12.5% (m/v) KCl solution was added (as spectrochemical buffer), and the mixture was diluted with distilled water to 25 mL. These solutions were analyzed. For each ferrite, reference solutions were also prepared according to its expected stoichiometric composition.

2.3. TGA Measurement. The process of a spinel phase formation in ZnFe_2O_4 was studied by thermogravimetric analysis (TGA) on a Perkin-Elmer TGS-2 instrument. A specimen of about 7 mg was heated at a rate of 10 °C/min by use of a platinum sample holder in a dynamic air flow (30 cm³/min), from room temperature up to 800 °C.

2.4. X-ray Data Collection. A Philips PW1710 automated X-ray powder diffractometer was used for the XRPD data collection. The diffractometer was equipped with a Cu tube, graphite monochromator and Xe-filled proportional counter. The generator was set up on 40 kV and 32 mA. Divergence and receiving slits were 1° and 0.1 mm, respectively. The diffractometer was calibrated with a silicon standard sample. Powders were back-loaded in an aluminum sample holder. Data for the Rietveld refinement were collected in a step scan mode between 15 and 135° 2θ at every 0.03° 2θ . The counting time was fixed to 20.7 s/step for all specimens except for ZnFe_2O_4 , where the counting time was 14.7 s.

2.5. Rietveld Refinement Procedure. The collected XRPD data of ZnFe_2O_4 , MnFe_2O_4 , and Mn–Zn ferrites were refined in the space group $Fd\bar{3}m$ and spinel type structure, starting from the model given by the literature.¹⁶ The refinement was performed with the Fullprof program.¹⁷ The TCH pseudo-Voigt profile function was used. To take into account instrumental broadening, the XRPD pattern of a standard BaF_2 specimen¹⁸

($U = 0.010\ 60$; $V = -0.014\ 35$; $W = 0.007\ 22$; $X = 0.047\ 31$; $Y = 0.047\ 21$) was fitted by the convolution to the experimental TCH pseudo-Voigt function. Although the BaF_2 standard specimen contains some defects, their influence on X-ray line broadening is negligible comparing to our ultrafine powder specimens.

The full width at half-maximum (fwhm) parameters of the Gaussian (H_G) and Lorentzian (H_L) components of the peak profile that we have used have an angular dependence given by¹⁹

$$H_G^2 = [U + (1 - \xi)^2 D_{\text{ST}}^2(\alpha_D)] \tan^2 \theta + V \tan \theta + W \quad (1)$$

$$H_L = [X + \xi D_{\text{ST}}(\alpha_D)] \tan \theta + \frac{Y}{\cos \theta} \quad (2)$$

In the present work, we have used the instrumental resolution function and therefore parameters V and W were fixed to zero. The rest of parameters in the above formula have a meaning in terms of strains (U , α_D , X) or size (Y). The function $D_{\text{ST}}(\alpha_D)$, after Stephens,²⁰ is given by

$$D_{\text{ST}}^2(\alpha_D) = 10^{-8} 8 \ln 2 \left(\frac{180}{\pi} \right)^2 \frac{\sigma^2(M_{hkl})}{M_{hkl}^2} \quad (3)$$

where $\sigma^2(M_{hkl})$ is

$$\sigma^2(M_{hkl}) = \sum_{HKL\{H+K+L=4\}} S_{HKL} h^H k^K l^L \quad (4)$$

The α_D s are the set of parameters S_{HKL} . Although 15 parameters may be refined (for the triclinic case), for the $m\bar{3}m$ symmetry only two independent parameters, S_{400} and S_{220} , are refined as previously done for Rb_3C_{60} .²⁰ The parameter ξ is a mixing coefficient that serves to mimic Lorentzian contribution to strains.

From the X-ray line broadening analysis, the apparent crystallite sizes and strains were calculated for each reflection:

$$\text{App - size} = \frac{1}{\beta_{\text{size}}} \quad (\text{angstroms}) \quad (5)$$

$$\text{App - strain} = \frac{1}{2} \beta_{\text{strain}} d_{hkl} (10^{-4}) \quad (6)$$

β_{size} is obtained from the size parameters contributing to the fwhm:

$$\text{fwhm}(\text{Lorentzian - size}) = H_{\text{LZ}} = \frac{Y}{\cos \theta} \quad (7)$$

β_{strain} is obtained from the strain parameters contributing to the fwhm:

$$\text{fwhm}^2(\text{Gaussian - strain}) = H_{\text{GS}}^2 = [U + (1 - \xi)^2 D_{\text{ST}}^2(\alpha_D)] \tan^2 \theta \quad (8)$$

$$\text{fwhm}(\text{Lorentzian - strain}) = H_{\text{LS}} = [X + \xi D_{\text{ST}}(\alpha_D)] \tan \theta \quad (9)$$

Both β_{size} and β_{strain} are deduced from these TCH parameters according to procedures described elsewhere.¹⁹ The standard deviations appearing in the global average apparent size and strain are calculated by use of the different reciprocal lattice directions. It is a measure of the degree of anisotropy, not of the estimated error.

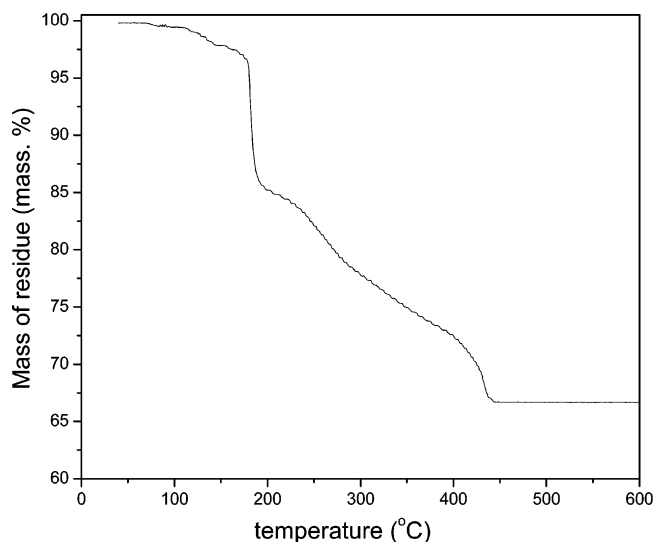


Figure 1. TGA curve for ZnFe_2O_4 spinel.

To avoid high correlation between parameters, some of them were refined separately: isotropic displacement parameters and site occupation parameters (N), Gauss (U) and Lorenz (X and Y) full widths at half-maximum (fwhm) parameters. The backgrounds were refined by use of selected points (both intensity and 2θ position). Number of selected points ranges between 18 for ZnFe_2O_4 and 11 for $\text{Zn}_{0.70}\text{Mn}_{0.23}\text{Fe}_{1.89}\text{O}_4$. Asymmetry of the X-ray diffraction lines was modeled up to $65^\circ 2\theta$. One or two asymmetry parameters (Asy_1 and Asy_3) were sufficient for successful refinement. Due to a relatively small number of reflections (86), coefficients S_{400} , S_{220} , and ξ (ξ = Lorentzian anisotropic strain mixing parameter) were refined one by one.

3. Results and Discussions

3.1. Formation and Chemical Composition of Ultrafine Powders. We have used acetylacetonato complexes as the precursors for the ultrafine ferrites preparation. In comparison with the classical ceramic method, where sintering temperatures are above 1000°C , thermal decomposition of the complexes occurs at relatively low temperatures. We have used a similar method of synthesis for obtaining NiFe_2O_4 .⁸ The TEM analysis⁸ showed that the ultrafine powder of NiFe_2O_4 consists of spherical particles with an average particle size of less than 20 nm. Consequently, we can assume that particle size of the samples under consideration is in the same range.

The synthesis process was checked by thermogravimetric analysis (TGA) of ZnFe_2O_4 sample (Figure 1). On the basis of the TGA curve, the temperature corresponding to the formation of spinel phase was determined to be 446°C . The TGA curve shows a mass loss in the range $20\text{--}450^\circ\text{C}$ with a residual mass of 66.7%. The thermal decomposition is a complex process where the mass loss occurs in four steps. The first step, dehydration of complex, takes place below 145°C . Sharp transition at about 180°C is induced by separation of gaseous products. Then, probably, networking of anhydrous complexes occurs in two steps at about 250 and 425°C (not resolved quite well) and the complete reaction ends at about 450°C , where spinel phase is formed. A similar thermogravimetric trace was found for MgFe_2O_4 , where the same synthesis method was used.²¹

All Zn–Mn ferrite specimens were single-phase spinels. In the case of ZnFe_2O_4 , two crystalline phases were found: 97.9-

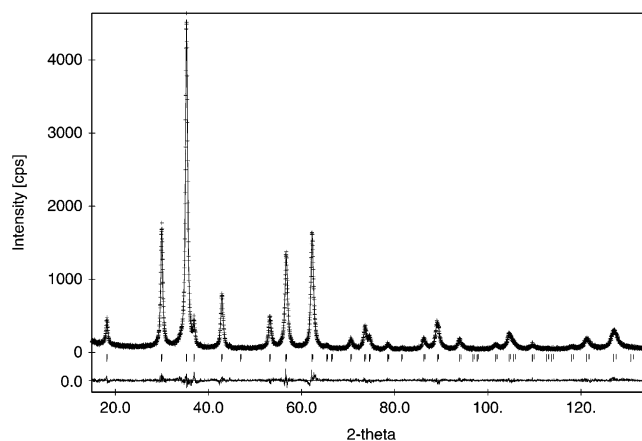


Figure 2. Comparison of observed (cross) and calculated (solid line) intensities for $\text{Zn}_{0.70}\text{Mn}_{0.23}\text{Fe}_{1.89}\text{O}_4$. The difference pattern appears below. The vertical bars, at the bottom, indicate reflection position.

(6%) spinel phase and 2.1(2)% $\alpha\text{-Fe}_2\text{O}_3$, i.e., hematite (values in parentheses are estimated standard deviations, esd). Quantitative composition of the two-phase system was obtained from the Rietveld refinement procedure. MnFe_2O_4 spinel contains a few percent ($I/I_{\text{max}} < 14\%$) of some unidentified phase.

The results of spectroscopic analysis indicated the existence of nonstoichiometry in Zn–Mn ferrites. The compositions of ternary samples are $\text{Zn}_{0.70}\text{Mn}_{0.23}\text{Fe}_{1.89}\text{O}_4$ (S1), $\text{Zn}_{0.41}\text{Mn}_{0.50}\text{Fe}_{1.84}\text{O}_4$ (S2), and $\text{Zn}_{0.18}\text{Mn}_{0.67}\text{Fe}_{1.85}\text{O}_4$ (S3). Though most spinels are stoichiometric, nonstoichiometry is not so rare. Some preparation procedures gave deviation of stoichiometry from an expected formula unit, $\text{Zn}^{2+}_{1-x}\text{Mn}^{2+}_x\text{Fe}^{3+}_2\text{O}_4$.^{22–24} In such spinel ferrites the iron ion is mostly in Fe^{3+} state and manganese ion in Mn^{2+} state, because it is more difficult to oxidize Mn^{2+} into Mn^{3+} than Fe^{2+} into Fe^{3+} .²⁴ Nonstoichiometry is a consequence of the facts that the iron and manganese cations can change their valence state and occupy both tetrahedral and octahedral sites. In the next section we will analyze possible cation oxidation states in nonstoichiometric Zn–Mn ferrites on the basis of cation distribution, cation–anion bond lengths, and Shannon ionic radii.

3.2. Crystal Structure, Cation Distribution, and Cation Valences. The results of the Rietveld refinement listed in Table 1 (and Figure 2) indicate good agreement between the structure model and experimental data. The estimated standard deviations of the refined parameters are sufficiently low to enable clear conclusions about cation distribution and to give some ideas about their oxidation states (see below). The small amount of hematite present in the ZnFe_2O_4 spinel does not influence conclusions given below.

The cation distribution in 8a and 16d crystallographic sites was investigated by the refinement of the occupation numbers (N). In ZnFe_2O_4 , occupation numbers for 8a and 16d sites were coupled and varied by one code word, keeping the stoichiometric ratio fixed. In ternary samples all possible combinations of cation distribution were examined. The criteria for the most probable distributions, reported here, were the lowest values of the agreement factors.

Values of occupation numbers indicate a partially inverse distribution in ZnFe_2O_4 , $(\text{Zn}_{1-\alpha}\text{Fe}_\alpha)_\text{A}[\text{Zn}_\alpha\text{Fe}_{2-\alpha}]_\text{B}$, where the inversion parameter α is 0.140(1). In nanosized ZnFe_2O_4 the degree of inversion was different, depending on the sample preparation method and on the thermal treatment.¹⁰ We have found cation distribution to be normal in MnFe_2O_4 where Mn^{2+} ions occupy 8a sites while Fe^{3+} ions are at 16d sites. A different

TABLE 1: Rietveld Refinement Results for Cation-Deficient $\text{Zn}_x\text{Mn}_y\text{Fe}_z\text{O}_4^a$

crystal system: face centered cubic	space group: $\text{Fd}\bar{3}m$ (227)				
Composition	ZnFe_2O_4	$\text{Zn}_{0.70}\text{Mn}_{0.23}\text{Fe}_{1.89}\text{O}_4$	$\text{Zn}_{0.41}\text{Mn}_{0.50}\text{Fe}_{1.84}\text{O}_4$	$\text{Zn}_{0.18}\text{Mn}_{0.67}\text{Fe}_{1.85}\text{O}_4$	MnFe_2O_4
lattice parameter a (Å)	8.437 97(7)	8.4330(1)	8.438 13(9)	8.474 80(8)	8.4983(2)
cation–anion distances d (Å)					
$d(\text{M}_{8a}-\text{O})^b$	$1.965(2) \times 4$	$1.955(2) \times 4$	$1.931(2) \times 4$	$1.938(1) \times 4$	$2.046(3) \times 4$
$d(\text{M}_{16d}-\text{O})$	$2.033(2) \times 6$	$2.037(2) \times 6$	$2.051(2) \times 6$	$2.061(1) \times 6$	$2.013(3) \times 6$
oxygen parameter u	0.2594(2)	0.2588(2)	0.2571(2)	0.2570(2)	0.2640(3)
temperature factors U_{eq} (Å ²)					
U_{8a}	0.0060(3)	0.0079(3)	0.0116(4)	0.0144(4)	0.0191(6)
U_{16d}	0.0063(4)	0.0076(3)	0.0084(3)	0.0112(3)	0.0191(6)
U_{32e}	0.0093(8)	0.0210(8)	0.0248(9)	0.0283(9)	0.0191(6)
occupation parameters N					
$N(\text{Zn})_{8a}$	0.2151(3)	0.1761(5)	0.1024(3)	0.0457(3)	
$N(\text{Fe})_{8a}$	0.0349(3)				
$N(\text{Mn})_{8a}$		0.0569(5)	0.1247(3)	0.1687(3)	0.25
$N(\text{Zn})_{16d}$	0.0349(3)				
$N(\text{Fe})_{16d}$	0.4651(3)	0.4726(5)	0.4575(3)	0.4635(3)	0.5
$N(\text{Mn})_{16d}$					
$N(\text{O})_{32e}$	1.0	1.0	1.0	1.0	1.0
profile parameters					
U	0.041(4)	0.041(8)	0.065(9)	0.066(9)	0.08(3)
X	0.129(8)	0.15(1)	0.26(1)	0.21(1)	0.34(3)
Y	0.211(3)	0.202(5)	0.218(6)	0.172(5)	0.04(1)
Asy_1	−0.040(2)	−0.022(2)	−0.32(2)	−0.31(3)	−0.50(7)
Asy_3			−0.57(5)	0.58(5)	1.0(2)
average apparent size (Å)	277(10)	146(7)	146(2)	204(1)	128(4)
average mixing strain $\times 10^3$	1.4(3)	1.5(2)	2.6(1)	2.4(1)	4.0(4)
anisotropic strain parameters					
S_{400}	0.039(6)	0.040(6)	0.045(7)	0.021(3)	0.022(1)
S_{220}	−0.19(2)	−0.20(1)	−0.21(3)	−0.025(6)	−0.032(3)
Ξ	0.06(3)	0.12(3)	0.15(4)	0.38(6)	1.9(1)
agreement factors					
cR_p (%)	11.48	12.96	14.98	15.67	27.14
cR_{wp} (%)	14.33	10.38	12.13	13.43	23.88
R_B (%)	1.72	1.80	2.20	2.89	9.40
χ^2	1.28	1.39	1.51	1.42	3.09
D	1.28	1.40	1.53	1.44	3.09

^a Crystal system: face-centered cubic. Space group $\text{Fd}\bar{3}m$ (227). ^b M denotes Zn, Mn, and Fe cations in 8a and 16d sites, respectively.

distribution was found in nanosized Mn ferrite: partially inverse, with significant percentage of Mn^{2+} at octahedral sites.²⁵ It has also been argued that the cation distribution in MnFe_2O_4 nanopowders prepared by coprecipitation depends on the crystallite size.²⁶

The elemental analysis shows a cation deficit in all Zn–Mn ferrite samples; that is, formula units are $\text{Zn}_x\text{Mn}_y\text{Fe}_z\Box_\delta\text{O}_4$, where $\delta = 0.18\text{--}0.30$. The sum of the refined occupation numbers is in agreement, within 3 esd, with the results of spectroscopic analysis. In nonstoichiometric Zn–Mn ferrites, the 16d sites are occupied exclusively by Fe^{3+} , while 8a sites are occupied by Zn^{2+} and Mn (Table 1). In spinel compounds Zn^{2+} ion has the largest preference for tetrahedral sites, while iron and manganese ions can occupy both sites, but not in all oxidation states (Mn^{3+} could be found only in octahedral coordination).^{27,28} Sum of occupation numbers for cations in 8a and 16d positions (Table 1) indicates that vacancy concentration is approximately the same at both sites for samples S1 and S2. In S3 sample there are more vacancies at tetrahedral sites. Thus, vacancy distribution is random, $(\text{Zn}_x\text{Mn}_y\Box_\epsilon)_{8a}[\text{Fe}_z\Box_\nu]_{16d}$.

Several papers deal with the cation distribution in spinel structure.²⁹ However, to our best knowledge a systematic analysis of vacancy distribution in spinels has not yet been done. We briefly discuss this topic via some examples. The cation distribution in $\gamma\text{-Fe}_2\text{O}_3$ ($\text{Fe}_{2.67}\text{O}_4$) is 8 Fe^{3+} at 8a sites and 13^{1/3} Fe^{3+} at 16d sites.³⁰ Hence, it can be concluded that vacancy distribution is preferential at 16d sites. In mechanically activated

nanosized Zn ferrite, vacancies are present at tetrahedral sites and there is overpopulation of cations in octahedral sites.³¹

Lattice parameter a versus manganese concentration has a nonlinear dependence (Table 1), as a consequence of cation distribution (induced by nonstoichiometry) and a polyvalent state of Mn and Fe. For a spinel compound, calculated cation–anion bond lengths d are a function of unit cell parameter and a fractional coordinate of oxygens. The observed nonlinearities in d vs Mn concentration for both octahedral $d(\text{M}_{16d}-\text{O})$ and tetrahedral $d(\text{M}_{8a}-\text{O})$ distances (Table 1) are due to (a) partial reduction of Fe^{3+} to Fe^{2+} and/or partial oxidation of Mn^{2+} to Mn^{3+} and Mn^{4+} , (b) cation distribution, and (c) coupled effect of a and b.

On the basis of cation–anion bond lengths and cation distributions, we can assume possible oxidation states of Fe and Mn in Zn–Mn ferrites. From the chemical formulas it can be seen that sum of the net formal charges in the case that all iron are Fe^{3+} and all manganese are Mn^{2+} does not stand for ternary spinel specimens, suggesting partial reduction of iron from Fe^{3+} to Fe^{2+} and/or oxidation of Mn^{2+} into Mn^{4+} . During the refinement Mn was always found to populate the tetrahedral 8a position (Table 1), and therefore we have excluded the possibility of Mn^{2+} oxidation into Mn^{3+} . In tetrahedral coordination Mn is found in oxidation states +2 and +4.³² By taking into account the percentage of Zn and Mn cations at 8a sites, and from the contribution of $d(\text{Mn}-\text{O})$ into $d(\text{M}_{8a}-\text{O})$, the percentage of Mn^{2+} and Mn^{4+} ions at tetrahedral sites was

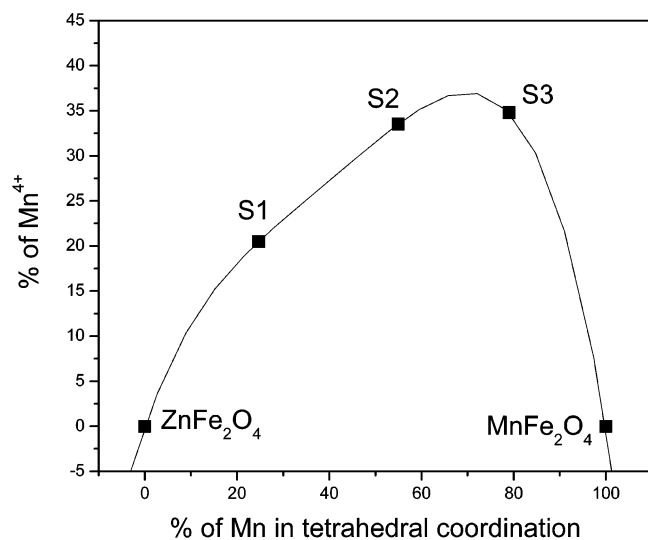


Figure 3. Percentage of Mn⁴⁺ versus percentage of Mn in tetrahedral coordination for samples under consideration (see text). The line is a guide for the eyes.

calculated. The values of used ionic radii were $r^{\text{IV}}(\text{Mn}^{2+}) = 0.66 \text{ \AA}$, $r^{\text{IV}}(\text{Mn}^{4+}) = 0.39 \text{ \AA}$, $r^{\text{IV}}(\text{Zn}^{2+}) = 0.60 \text{ \AA}$, and $r^{\text{IV}}(\text{O}^{2-}) = 1.38 \text{ \AA}$.^{28,32} In the Mn-poor sample, $\text{Zn}_{0.70}\text{Mn}_{0.23}\text{Fe}_{1.89}\text{O}_4$, the majority of Mn ($\approx 84\%$) is in the +4 oxidation state. For the $\text{Zn}_{0.41}\text{Mn}_{0.50}\text{Fe}_{1.84}\text{O}_4$ sample, Mn has oxidation states +2 ($\approx 39\%$) and +4 ($\approx 61\%$). In the Mn-rich sample, $\text{Zn}_{0.18}\text{Mn}_{0.67}\text{Fe}_{1.85}\text{O}_4$, the quantities of Mn ions in +2 and +4 oxidation states are $\approx 56\%$ and $\approx 44\%$, respectively. In MnFe_2O_4 , 100% of Mn is in the +2 oxidation state. Finally, we discuss the ratio of Mn⁴⁺ versus overall Mn concentration (% Mn⁴⁺ vs % Mn) with respect to the change of chemical composition. With % Mn⁴⁺ we denote the percentage of Mn⁴⁺ in manganese occupying tetrahedral sites, while % Mn denotes the percentage of manganese in tetrahedral sites. Dependence of % Mn⁴⁺ versus % Mn is shown in Figure 3. In Zn-rich ternary samples % Mn⁴⁺ increases with the increase in % Mn. A maximum is reached at % Mn ≈ 70 , and with the further increase in % Mn (Mn-rich samples) there is an abrupt lowering of % Mn⁴⁺ (Figure 3). Comparing the values of d for 16d sites (Table 1) with $d(\text{Fe}^{3+}\text{--O}) = 2.045 \text{ \AA}$ and $d(\text{Fe}^{2+}\text{--O}) = 2.18 \text{ \AA}$,³² we can conclude that in S1 and S2 samples all Fe ions within experimental error are in oxidation state +3. For the S3 sample there is an indication of the presence of Fe²⁺ ions in a very small percentage. Thus, it is easier to oxidize Mn from +2 into +4 than to reduce Fe from +3 into +2. The Zn has a +2 stable valence.

For ZnFe_2O_4 and MnFe_2O_4 binary ferrites, crystallite size- and strain-induced X-ray line broadening analysis indicates larger crystallites and smaller strains in ZnFe_2O_4 (Table 1) than in MnFe_2O_4 . For ternary (Zn,Mn) ferrites, crystallites are bigger in S3 than in S1 and S2, while strains are higher in S2 and S3 than in S1. Values that measure degree of anisotropy of apparent crystallite size and strain (in parentheses, Table 1) indicated that only X-ray line broadening due to the strain effect is significantly anisotropic. For both binary ferrites, strain-induced X-ray line broadening is significantly anisotropic, especially for ZnFe_2O_4 (2 times higher than for MnFe_2O_4). For ternary ferrites, strain-induced X-ray line broadening is less anisotropic than in binary ferrites and decreases with the increase in vacancy concentration δ . To define the strain-induced anisotropy of X-ray line more precisely, broadening parameters S_{400} , S_{220} , and ξ (Table 1) were refined. A three-dimensional representation of

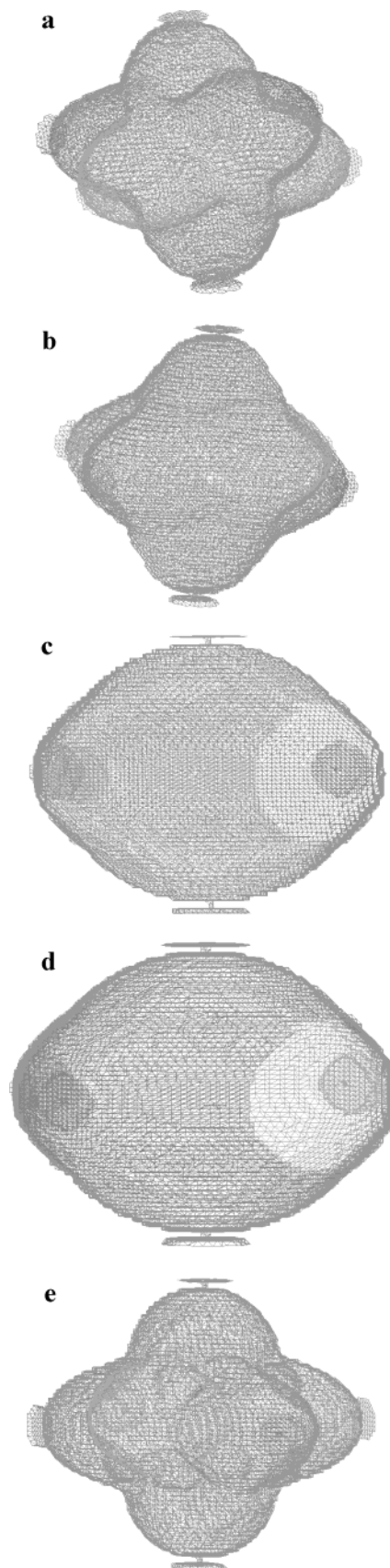


Figure 4. Three-dimensional representation of strain in (a) ZnFe_2O_4 , (b) S1, (c) S2, (d) S3, and (e) MnFe_2O_4 .

strains in title compounds is presented in Figure 4 (see also Supporting Information, i.e., files with *.str and *.mic parameters).

4. Conclusion

A new synthesis route based on the thermal decomposition of appropriate complex compounds with acetylacetonate ligands was applied to prepare ultrafine powders of Zn, Mn, and Zn–Mn ferrites. Mixed Zn–Mn ternary ferrites are nonstoichiometric with large vacancy concentration. The ZnFe_2O_4 is a partial inverse binary spinel, with the degree of inversion $\alpha = 0.140(1)$, while the MnFe_2O_4 is a normal binary spinel. Analysis of cation distribution in mixed ternary spinels reveals that Zn and Mn occupy tetrahedral (8a) sites, while Fe occupy octahedral (16d) sites. Vacancy distribution is found to be random. Only in ternary spinels does partial oxidation of Mn^{2+} into Mn^{4+} occur. X-ray line broadening due to the crystallite size effect is isotropic, while X-ray line broadening due to the strain effect is significantly anisotropic in title compounds. Strain anisotropy is higher for binary than for ternary ferrites. With growing vacancy concentration δ , the strain anisotropy in ternary ferrites decreases.

Acknowledgment. The Serbian Ministry of Science, Technology and Development has financially supported this work through Projects 2022, 1253, and 1995. We thank Professor Dejan Poleti and Dr. Ivana Radosavljevic-Evans for helpful discussions and Dr. Zorica Kacarevic-Popovic for performing TGA measurements.

Supporting Information Available: CIF files (profile data included as separate files) for all refined XRPD patterns and phases, microstructure analysis files (*.mic), and strain data files containing strain along any direction in space (*.str). This information is available free of charge via the Internet at <http://pubs.acs.org>.

References and Notes

- (1) Jeyadevan, B.; Chinnasamy, C. N.; Shinoda, K.; Tohji, K.; Oka, H. *J. Appl. Phys.* **2003**, *93*, 8450.
- (2) Caizer, C. *J. Magn. Magn. Mater.* **2002**, *251*, 304.
- (3) Kim, W. C.; Kim, S. J.; Kim, C. S. *J. Appl. Phys.* **2002**, *91*, 7607.
- (4) Huang, C.; Matijevic, E. *Solid State Ionics* **1996**, *84*, 249.
- (5) Anwar, A.; Fujiwara, T.; Song, S.; Yoshimura, M. *Solid State Ionics* **2002**, *151*, 419.

- (6) Miyagawa, C.; Haneda, K.; Goto, K. Jpn. Kokai Tokkyo Koho JP 63 25,224, 1988.
- (7) Miyagawa, C.; Haneda, K.; Goto, K.; Kawamoto, O. Jpn. Kokai Tokkyo Koho JP 63 210,031, 1988.
- (8) Nikolic, A. S.; Cvetkovic, N.; Djuric, S.; Puzovic, J.; Pavlovic, M. *B. Mater. Sci. Forum* **1998**, 282–283, 199 and references therein.
- (9) Hastings, J. M.; Corliss, L. M. *Rev. Mod. Phys.* **1953**, *25*, 114.
- (10) Goya, G. F.; Rechenberg, H. R.; Chen, M.; Yelon, W. B. *J. Appl. Phys.* **2000**, *87*, 8005 and references therein.
- (11) Rath, C.; Mishra, N. C.; Anand, S.; Das, R. P.; Sahu, K. K.; Upadhyay, C.; Verma, H. C. *Appl. Phys. Lett.* **2000**, *76*, 475.
- (12) Fatemi, D. J.; Harris, V. G.; Chen, M. X.; Malik, S. K.; Yelon, W. B.; Long, G. J.; Mohan, A. *J. Appl. Phys.* **1999**, *85*, 5172.
- (13) Fatemi, D. J.; Harris, V. G.; Browning, V. M.; Kirkland, J. P. *J. Appl. Phys.* **1988**, *83*, 6867.
- (14) Charles, R. G.; Pawlikowski, M. A. *J. Phys. Chem.* **1958**, *62*, 440.
- (15) Kuzmanović, M.; Pavlović, M. S.; Marinković, M. *Spectroscopy Lett.* **1996**, *29*, 208.
- (16) Scharner, S.; Weppner, W.; Schmid-Beurmann, P. *J. Sol. State Chem.* **1997**, *134*, 170.
- (17) Rodriguez-Carvajal, J. FullProf computer program; <ftp://charybde.saclay.cea.fr/pub/divers/fullprof.98/windows/winf98.zip>, 1998.
- (18) Louër, D.; Langford, J. I. *J. Appl. Crystallogr.* **1988**, *21*, 430.
- (19) http://www-llb.cea.fr/fullweb/fp2k/fp2k_divers.htm (file Fullprof-Manual.zip).
- (20) Stephens, P. W. *J. Appl. Crystallogr.* **1999**, *32*, 281.
- (21) Antic, B.; Rodic, D.; Nikolic, A. S.; Kacarevic-Popovic, Z.; Karanović, Lj. *J. All. Compounds* **2002**, *336*, 286.
- (22) Topfer, J.; Liu, L.; Dieckmann, R. *Solid State Ionics* **2003**, *159*, 397.
- (23) Samoilenko, Z. A.; Paschenko, V. P.; Abramov, V. S.; Ivankhenko, N. N. *Sov. Phys. Solid State* **2001**, *43*, 1556.
- (24) Razzitte, A. C.; Jacobo, S. E.; Fano, W. G. *J. Appl. Phys.* **2000**, *87*, 6232.
- (25) Chen, J. P.; Sorensen, C. M.; Klabunde, K. J.; Hadjipanayis, G. C.; Devlin, E.; Kostikas, A. *Phys. Rev.* **1996**, *54*, 9288.
- (26) Muroi, M.; Street, R.; McCormick, P. G.; Amighian, J. *Phys. Rev.* **2001**, *B63*, 184414 and references therein.
- (27) Navrotsky, A.; Kleppa, J. O. *J. Inorg. Nucl. Chem.* **1967**, *29*, 2701.
- (28) Scordari, F. Ionic crystals. In *Fundamentals of Crystallography*; Giacovazzo, C., Ed.; IUCr Texts on Crystallography 2; Oxford University Press Inc.: New York, 1993.
- (29) Krupicka, S.; Novak, P. Oxide Spinel. In *Ferromagnetic Materials*, Vol. 3; Wohlfarth, E. P., Ed.; North-Holland Publishing Co.: New York, 1982.
- (30) Novikov, S. I.; Lebedeva, E. M.; Shtol'ts, A. K.; Yurchenko, L. I.; Tsurin, V. A.; Barinov, B. A. *Fiz. Tverdogo Tela* **2002**, *44*, 119.
- (31) Oliver, S. A.; Harris, V. G.; Hamdeh, H. H.; Ho, J. C. *Appl. Phys. Lett.* **2000**, *76*, 2761.
- (32) Shanon, R. D. *Acta Crystallogr.* **1976**, *A32*, 751.